Three-body fragmentation dynamics of CH_3CCH^{3+} investigated by 50-keV/u Ne^{8+} impact: Comparison with its isomer ion $CH_2CCH_2{}^{3+}$

Hang Yuan,[1,2] Zhongfeng Xu,[1] Shenyue Xu,[2,3,*] Chao Ma,[4] Zhen Zhang,[1] Dalong Guo,[2,3] Xiaolong Zhu,[2,3] Dongmei Zhao,[2] Shaofeng Zhang,[2,3] Shuncheng Yan,[2,3] Yong Gao,[2,3] Ruitian Zhang,[2,3] and Xinwen Ma[2,3,†]

[1]*School of Physics, Xi'an Jiaotong University, Xi'an 710049, China*

[2]*Institute of Modern Physics, Chinese Academy of Sciences, Lanzhou 730000, China*

[3]*School of Nuclear Science and Technology, University of Chinese Academy of Sciences, Beijing 100049, China*

[4]*Foundation Department, Engineering University of PAP, Xi'an 710086, China*

(Received 19 August 2021; accepted 1 February 2022; published 22 February 2022)

The three-body fragmentation dynamics of propyne (CH_3CCH) to $H^+ + CH^+ + C_2H_2{}^+$ and $H^+ + CH_2{}^+ + C_2H^+$ is investigated by 50-keV/u Ne^{8+} ion impact. Employing the reaction microscope, all three ionic fragments are detected in coincidence, and the momentum vector as well as kinetic energy of each fragment is obtained. By analyzing the momentum and kinetic energy correlation between different fragments, various fragmentation mechanisms are identified, and the relative ratio of each mechanism is determined. We find that the concerted fragmentation with CH and CC bonds breaking simultaneously and the sequential pathway with CH breakage prior to the CC breakage are the major contributions to both channels. In contrast, the sequential pathway with CC breakage prior to CH breakage was found to make a minor contribution only to the $H^+ + CH^+ + C_2H_2{}^+$ channel. In addition, we compare the present results for CH_3CCH with CH_2CCH_2 published in Ma *et al.* [C. Ma, S. Xu, D. Zhao, D. Guo, S. Yan, W. Feng, X. Zhu, and X. Ma, Phys. Rev. A **101**, 052701 (2020)]. The location of the CH and CC bonds' breakage, either from distinct C atoms or from the same C atom, leads to similar dissociation mechanisms but different ionic fragments for the two isomers.

DOI: 10.1103/PhysRevA.105.022814

I. INTRODUCTION

Fragmentation dynamics of multicharged polyatomic molecules has been a striking topic in recent years. Besides the fundamental interest in physics and chemistry, such a process also plays important roles in many application fields, such as plasmas physics [1], radiation damage of biological tissues [2], and chemistry of planetary atmosphere [3]. The multicharged molecular cations can be generated when isolated molecules interact with high-energy radiation, such as ions, electrons, x rays, and intense laser fields. Such multicharged molecular cations are usually unstable and can dissociate to pieces. Among various dissociation channels, the three-body fragmentation dynamics have been frequently studied.

In such processes, at least two covalent bonds break either simultaneously or sequentially, leading to complicated competition between different mechanisms. Taking the advantage of the improved momentum imaging techniques, the momentum vectors of all ionic fragments can be measured in multicoincidence. This makes it possible to visualize the three-body fragmentation dynamics in detail by analyzing the momentum and kinetic energy (KE) correlation between different fragments. The triatomic molecules such as CO_2 [4–9], NO_2 [4,10,11], OCS [4,12–16], and H_2O [17] have been chosen as prototype systems to investigate the mechanisms of three-body fragmentation in the past decades. Besides, the three-body fragmentation of hydrocarbon molecules like CH_4 [18–20], C_2H_2 [21–25], C_2H_4 [26,27], and C_6H_6 [28,29] have also been investigated.

Propyne (CH_3CCH) and allene (CH_2CCH_2) are two isomers of C_3H_4 that stably exist in nature. They are frequently chosen as the prototype for the study of isomer effects, i.e., the correlation between fragmentation dynamics and the molecular structure during ionization and dissociation [30–33]. Kusakabe *et al.* investigated the charge-transfer interaction between C_3H_4 and C^+ ion beam with keV energies. The measured cross section curves of the charge-transfer process exhibit apparent isomer effect that the cross sections for allene are much higher than propyne [31]. Scully *et al.* investigated the fragmentation of propyne and allene dications induced by electrons, and the unambiguous difference between the two isomers is observed in the partial double-ionization spectra over a broad projectile energy ranging from 25 to 1000 eV [32]. In a recent study, obvious isomer effects were identified in the direct two-body fragmentation resulting from either CC bond or CH bond breaking by 50-keV/u Ne^{8+} impact [33]. On the contrary, no isomer effect was observed in the delayed deprotonation dissociation [34].

In this study, we report the fragmentation dynamics of CH_3CCH to $H^+ + CH^+ + C_2H_2{}^+$ and $H^+ + CH_2{}^+ + C_2H^+$ investigated by 50-keV/u Ne^{8+} ion impact, and we focus on the isomer effects in the three-body fragmentation by comparing the dissociation dynamics of CH_3CCH with the results for CH_2CCH_2 published in Ref. [35]. In our recent study on

*s.xu@impcas.ac.cn
†x.ma@impcas.ac.cn

CH_2CCH_2, it was found that, besides the concerted fragmentation process, the sequential processes with either CH bond or CC bond breaking in the first step also contribute to the $H^+ + CH_2^+ + C_2H^+$ channel, while the sequential fragmentation with CC bond breaking in the first step disappears in the $H^+ + CH^+ + C_2H_2^+$ channel [35]. In order to make an effective comparison between the two isomers, the measurements for propyne reported here were performed with the same experimental conditions as the measurement for allene reported in Ref. [35].

II. EXPERIMENT

The experiment was performed with the reaction microscope (also called cold target recoil-ion-momentum spectroscopy) [36–38] mounted at the 320-kV platform for multidisciplinary research with highly charged ions located at the Institute of Modern Physics, Chinese Academy of Sciences. Details of the experiment have been presented in Refs. [24,33–35]; only a brief introduction is given here. The well-collimated Ne^{8+} beam (∼1 mm in diameter) intersects with the CH_3CCH gas jet (∼2 mm in diameter) produced by supersonic expansion through a nozzle 30 μm in diameter. The driving pressure of the target is 1 bar. Under this condition, the gas jet contains almost only monomer, and the contribution of clusters is negligible. Three sets of electrostatic deflectors are mounted in front of the collision zone to steer and clean the projectile beam. After collision, the scattered projectile ions with different charge states are separated in position by a parallel electrostatic deflector. The Ne^{7+} ion which captures one electron from the target is recorded by a time- and position-sensitive detector. The ionic fragments are extracted by the uniform electric field which is perpendicular to the plane defined by the projectiles beam and the target beam. After passing the accelerating region and a field-free drift region, these ionic fragments are finally detected by another time- and position-sensitive detector. The scattered projectiles and ionic fragments are recorded in multicoincidence. The arrival time of the projectiles to the detector acts as the trigger signal for determining the absolute time-of-flight (TOF) of the ionic fragments.

The TOF information is used to distinguish the species of each ionic fragment, and thus different dissociation channels can be identified. The momentum vector of each ionic fragment is reconstructed according to the TOF and position information, and consequentially, the KEs are obtained. In addition, the momentum conservation condition is utilized to further eliminate the false coincidence.

The energy of projectile is chosen as 50-keV/u corresponding to the velocity of 1.4 a.u. At this energy, the interaction between the projectile and the target is dominated by the interaction between the projectile and the target electron, while the interaction between the projectile and the target nuclei is negligible. In the present study, we investigate the fragmentation dynamics of propyne trication (CH_3CCH^{3+}). The precursor ${C_3H_4}^{3+}$ trications are mainly produced through capturing one electron while ionizing the other two electrons by the projectile, i.e., the transfer ionization process [38]:

$$Ne^{8+} + C_3H_4 \rightarrow Ne^{7+} + {C_3H_4}^{3+} + 2e^-.$$

We consider the following two three-body fragmentation channels:

$${C_3H_4}^{3+} \rightarrow H^+ + CH^+ + {C_2H_2}^+, \quad \text{(I)}$$

$${C_3H_4}^{3+} \rightarrow H^+ + {CH_2}^+ + C_2H^+. \quad \text{(II)}$$

The data are displayed in Dalitz plots [35,39,40], Newton diagrams [4,12], and native frames [41,42].

In the Dalitz plot, the X and Y coordinates are defined as

$$X = \frac{P_b^2 - P_a^2}{\sqrt{3}\sum P_i^2}, \quad (1)$$

$$Y = \frac{P_c^2}{\sum P_i^2} - \frac{1}{3}. \quad (2)$$

where P_i ($i = a$, b, and c) denotes the momentum of the three ionic fragments H^+, CH^+, and ${C_2H_2}^+$ for channel I and H^+, ${CH_2}^+$, and C_2H^+ for channel II. Each point in the Dalitz plot reveals a specific momentum correlation among the three fragments.

The Newton diagram provides a more intuitive view of the relative relationships among three fragments. In this diagram, the momentum vector of the H^+ ion is set at 1.0 arb. unit along the x axis, while the momentum vectors of $C_2H_2^+$ and CH^+ (channel I) or of C_2H^+ and ${CH_2}^+$ (channel II) are normalized to that of H^+ and located in the upper and lower halves of the diagram, respectively.

In the native frames, all events are assumed to occur via a sequential pathway with a specific metastable intermediate dication (INT): $ABC^{3+} \rightarrow A^+ + BC^{2+} \rightarrow A^+ + B^+ + C^+$. Following such an assumption, the data are presented as a function of $\gamma_{\rm INT}$ and $\rm KER_{INT}$. Here γ is defined as the relative angle between the fragmentation axis of the first step in the center-of-mass (CM) frame of ABC which is equal to the laboratory frame and the fragmentation axis of the second step in the CM of BC. It is calculated by

$$\gamma = \arccos\left(\frac{\Delta\vec{P}_{\rm 1st} \cdot \Delta\vec{P}_{\rm 2nd}}{|\Delta\vec{P}_{\rm 1st}||\Delta\vec{P}_{\rm 2nd}|}\right). \quad (3)$$

Here $\Delta\vec{P}_{\rm 1st}$ is the difference between the momentum vectors of A^+ and the intermediate BC^{2+} in the CM of ABC, while $\Delta\vec{P}_{\rm 2nd}$ is the difference between the momentum vectors of B^+ and C^+ in the CM of BC^{2+},

$$\Delta\vec{P}_{\rm 1st} = \vec{P}_{\rm A} - (\vec{P}_{\rm B} + \vec{P}_{\rm C}), \quad (4)$$

$$\Delta\vec{P}_{\rm 2nd} = \left(\vec{P}_{\rm B} + \frac{m_{\rm B}}{m_{\rm BC}}\vec{P}_{\rm A}\right) - \left(\vec{P}_{\rm C} + \frac{m_{\rm C}}{m_{\rm BC}}\vec{P}_{\rm A}\right). \quad (5)$$

Here $\vec{P}_{\rm A}$, $\vec{P}_{\rm B}$, and $\vec{P}_{\rm C}$ are momentum vectors of the three fragments measured in the laboratory frame. $\rm KER_{INT}$ is the kinetic energy release in the second step in the CM of INT.

For the complete sequential process with the intermediate dication surviving much longer than the rotational period, this plot shows a uniform distribution along $\gamma_{\rm INT}$. As discussed later in the text, we use this uniform distribution of $\gamma_{\rm INT}$ to estimate the relative intensities of several competing channels even when two channels are overlapping in the Dalitz or Newton plots.

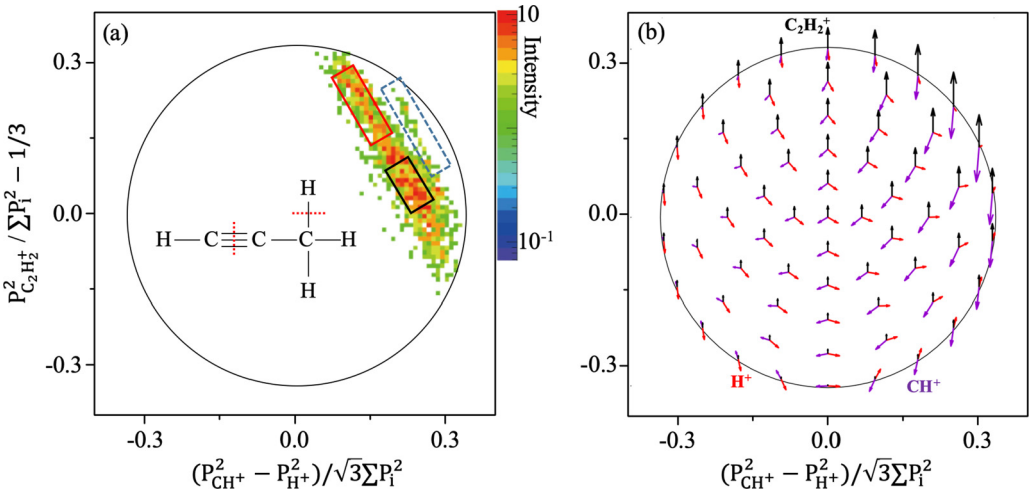

FIG. 1. Dalitz plot for the $H^+ + CH^+ + C_2H_2^+$ channel. (a) Experimental data. Black, red (gray) and blue (dashed) rectangles works as filters to deduce KE distributions of the fragments shown in Figs. 2(e)–2(g). The main contribution to the black rectangle is concerted fragmentation with an admixture from sequential pathway A. The red rectangle only contains the contribution of pathway A. Events inside the blue dashed rectangle are attributed to pathway B. The inset shows the chemical structure of CH_3CCH and the bond cleavage leading to this channel. (b) Calculated momentum correlations of the three ionic fragments as the function of Dalitz coordinates (X, Y). The red, purple, and black arrows represent the momentum vectors of the H^+, CH^+, and $C_2H_2^+$ ions, respectively.

III. RESULTS AND DISCUSSIONS

A. $H^+ + CH^+ + C_2H_2^+$ channel

The Dalitz plot for the $H^+ + CH^+ + C_2H_2^+$ channel is displayed in Fig. 1(a). The most intense region in this figure is labeled by the black rectangle. This region overlaps with an oblique stripe structure which is partly labeled by the red (gray) rectangle in Fig. 1(a). Besides, there is another stripe structure with weak intensity, as marked by the blue dashed rectangle. Figure 1(b) displays the calculated momentum correlations as the function of the Dalitz coordinates. The major contribution of the most intense region in Fig. 1(a) is attributed to direct fragmentation of CH_3CCH^{3+} to H^+, CH^+, and $C_2H_2^+$ with one CH bond and one CC bond breaking simultaneously [see insert in Fig. 1(a)], since as displayed in Fig. 1(b) the momentum correlations corresponding to this region are consistent with the initial configuration of the CH_3CCH molecule.

Figure 2(a) displays the Newton diagram of this channel. The momentum of H^+ is normalized to 1.0 arb. unit and fixed along the x axis, while the momentum vectors of the other two fragments, CH^+ and $C_2H_2^+$, are normalized to the momentum of H^+ and are plotted in the lower and upper half of the diagram, respectively. The intense regions in the top right and bottom left quadrants correspond to the intense region marked by the black rectangle in the Dalitz plot shown in Fig. 1(a), which originates from concerted fragmentation.

The semicircular structures marked by black solid lines correspond to the intense oblique stripes in Fig. 1(a). Along the intense oblique stripe shown in Fig. 1(a) (corresponding to the black solid circles in the Newton diagram), it can be seen in Fig. 1(b) that the angle between the momenta of CH^+ (purple arrow) and $C_2H_2^+$ (black arrow) rarely changes. In contrary, the angles between H^+ (red arrow) and the other two fragments changes significantly. Such a feature indicates that this structure arises from the sequential pathway with the proton emitted in the first step while the other fragments are emitted in the second step. Here we denote this fragmentation process as pathway A:

$$\begin{aligned} C_3H_4{}^{3+} &\rightarrow H^+ + C_3H_3{}^{2+}, && \text{step 1,} \\ C_3H_3{}^{2+} &\rightarrow CH^+ + C_2H_2{}^+, && \text{step 2.} \end{aligned} \qquad \text{(A)}$$

There is another semicircular structure with weak intensity which is marked by blue dashed cycles in Fig. 2(a). This structure corresponds to the events inside the blue dashed rectangle in Fig. 1(a). The semicircular structure indicates that another sequential pathway different from pathway A probably occurred. Since this channel involves the breaking of one CH bond and one CC bond, it is reasonable to assume that the semicircular structure with weak intensity is from the sequential pathway with CC bond breaking prior to the CH bond breaking, and the CH^+ is produced in the first step. We denote this fragmentation sequence as pathway B:

$$\begin{aligned} C_3H_4{}^{3+} &\rightarrow CH^+ + C_2H_3{}^{2+}, && \text{step 1,} \\ C_2H_3{}^{2+} &\rightarrow H^+ + C_2H_2{}^+, && \text{step 2.} \end{aligned} \qquad \text{(B)}$$

In Fig. 2(c) the events inside the blue dashed rectangle of Fig. 1(a) are displayed in the Newton diagram with the momentum of the CH^+ fixed, while the momenta of H^+ and $C_2H_2^+$ are normalized to that of CH^+. This figure also shows semicircular structures which are typical features of the sequential fragmentation process.

The assignment of sequential pathways A and B are confirmed by the KE distributions of the three fragments. Figures 2(e)–2(g) present the KE distributions of the three ionic fragments with the filters of the black, red (gray), and blue (dashed) rectangles in Fig. 1(a), respectively. As shown in Fig. 2(e), the KE of H^+ in pathway B is reduced to half of the KE of the concerted fragmentation and the sequential pathway A, demonstrating that the proton is emitted from

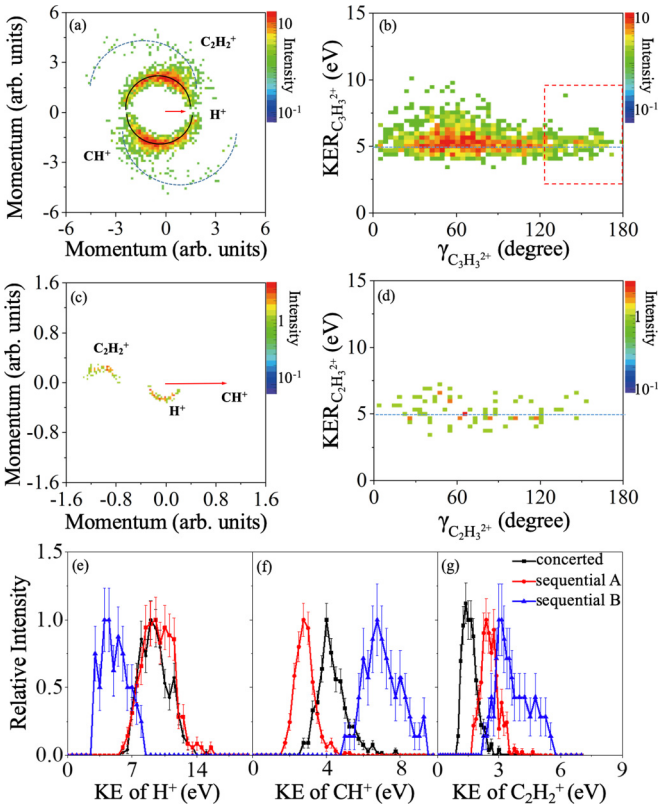

FIG. 2. (a) Newton diagram normalized to the momentum of H^+. (b) The γ_{INT} vs KER_{INT} plot for events outside the blue dashed rectangle in Fig. 1(a), assuming $C_3H_3^{2+}$ as the intermediate dication. The red dashed rectangle in this figure arises exclusively from pathway A. Counts inside this rectangle are used to evaluate the total counts of pathway A. (c) Newton diagram normalized to the momentum of CH^+ for the events inside the blue rectangle in Fig. 1(a). Such events are assigned to pathway B. (d) The γ_{INT} vs KER_{INT} plot for events inside the blue dashed rectangle in Fig. 1(a) which are assigned to pathway B with the intermediate dication of $C_2H_3^{2+}$. (e)–(g) KE distributions of H^+, CH^+, and $C_2H_2^+$ with the Dalitz filters defined in Fig. 1(a). These curves are normalized to unity at the maximum.

the cation with a lower charge state. Namely, the proton is ejected from the intermediate dication $C_2H_3^{2+}$ in the second step. At the same time, the CH^+ from pathway B receives higher KE compared to the other two processes, which further confirms our assignment of pathway B [12,27,35]. In addition, the $C_2H_2^+$ from pathway B obtains more KE than pathway A as shown in Fig. 2(g). This is partly due to the fact that the KE obtained by intermediate dication in the first step is assigned among the two fragments in the second step proportional to their mass. Thus, in pathway B the $C_2H_2^+$ inherits 26/27 of the KE of the intermediate dication, which is higher than 26/39 for pathway A.

As observed in Figs. 1(a) and 2(a), the events of the concerted fragmentation and pathway A display a partial overlapping. Such overlapping makes it impossible to separate the two contributions and determine the branching ratios directly. We employ the native frame to estimate the branching ratios of different contributions. The events outside the blue dashed rectangle are plotted as a function of γ_{INT} vs KER_{INT} in Fig. 2(b), assuming that all such events come from sequential process pathway A with the intermediate dication $C_3H_3^{2+}$. Sequential pathway A results in a band distribution as marked with the blue dashed line along the γ axis, while the dense region with $\gamma = 60^\circ$ mainly comes from concerted fragmentation and overlaps with pathway A. Meanwhile, the events inside the red dashed rectangle are assumed to come completely from sequential pathway A. Thus the total number of events in pathway A can be obtained by extending this region to the whole 0° to 180° range. Figure 2(d) displays the γ_{INT} vs KER_{INT} plot for events inside the blue dashed rectangle by assuming the intermediate dications to be $C_2H_3^{2+}$. It shows a typical uniform distribution which confirms the assignment of events inside the blue dashed rectangle to pathway B. The number of concerted events is evaluated by subtracting pathway A and pathway B from the total count of this channel. In this way, the branching ratios of concerted fragmentation, pathways A and pathway B are determined to be 64±10%, 30±7%, and 6±4%, respectively. The errors are conservatively estimated by combined consideration of standard derivation of the counts and the uncertainty arising from the overlap between sequential and concerted processes.

B. $H^+ + CH_2^+ + C_2H^+$ channel

Figure 3 shows the Dalitz plots for the $H^+ + CH_2^+ + C_2H^+$ channel. As displayed in Fig. 3(a), the Dalitz plot for the $H^+ + CH_2^+ + C_2H^+$ channel shows a significant intense region (marked by black rectangle) overlapping with an oblique stripe. This intense region corresponds to the intense islands located in the lower and upper panels in the Newton diagram shown in Fig. 4(a). They are attributed to the concerted fragmentation process originating from the initial structure of the neutral target.

Besides the intense region, an oblique stripe structure can be observed, which is the typical feature of the sequential fragmentation. Along the oblique stripe structure, when the angle between the momenta of H^+ and CH_2^+ increases, the angle between the momenta of H^+ and C_2H^+ decreases, indicating that the H^+ is emitted independently in the first step. This structure corresponds to the semicirclar structure marked with black curve in Fig. 4(a), which comes into being since the intermediate molecular ion is rotated for a while rather than dissociating immediately. After the H^+ is emitted from the methyl group in the first step, the intermediate ion $C_3H_3^{2+}$ dissociates into CH_2^+ and C_2H^+ in the second step. We denote such a process as pathway C:

$$C_3H_4^{3+} \rightarrow H^+ + C_3H_3^{2+}, \qquad \text{step 1},$$
$$C_3H_3^{2+} \rightarrow CH_2^+ + C_2H^+, \qquad \text{step 2}. \qquad \text{(C)}$$

Figures 4(c)– 4(e) display the KE distributions of the three ionic fragments with different filters. The black and red curves correspond to the KE distributions of the black (mainly concerted fragmentation) and red (only pathway C) rectangles in Fig. 3(a), respectively. The KE of H^+ with two filters shows similar distributions with little discrepancy. In the concerted fragmentation process, H^+ moves fast away from CH_2^+ and C_2H^+, while CH_2^+ and C_2H^+ moves much slower than H^+ because of the comparatively small mass of H^+ compared

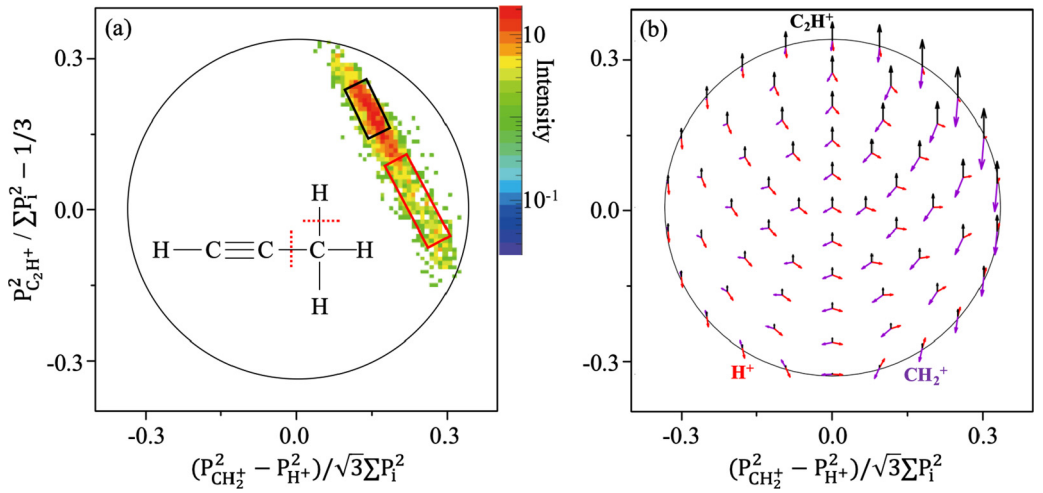

FIG. 3. Experimental and theoretical Dalitz plot for the $H^+ + CH_2^+ + C_2H^+$ channel. (a) Dalitz plot. Black and red (gray) rectangles are Dalitz filters used to deduce KE distributions of the fragments shown in Figs. 4(c)– 4(e). The black rectangle contains mixed contribution from both concerted fragmentation and sequential pathway C, while the red rectangle only includes the contribution of pathway C. The inset shows the chemical structure of CH_3CCH and the bond cleavage leading to this channel. (b) Calculated momentum correlations of the three ionic fragments as the function of Dalitz coordinates (X, Y). The red, purple, and black arrows represent the momentum vectors of the H^+, CH_2^+, and C_2H^+ ions, respectively.

to the other two fragments [43]. The similarity in the KE distributions of protons reflects that in the concerted process the movement of CH_2^+ and C_2H^+ during emission of H^+ is negligible, and the Coulomb potential experienced by H^+ is almost the same as that from the intermediate $C_3H_3^{2+}$ in the sequential pathway B. The KEs of CH_2^+ and C_2H^+ depend strongly on the Dalitz filters. The KE of CH_2^+ increases as the KE of C_2H^+ decreases. Such features support the assignment of pathway C, since the rotation of $C_3H_3^{2+}$ will modify the KEs of the fragments produced in the second step.

Figure 4(b) exhibits the γ_{INT} vs KER_{INT} plot for the $H^+ + CH_2^+ + C_2H^+$ channel by assuming $C_3H_3^{2+}$ as the intermediate dication. The most intense region with γ_{INT} around 100° includes the contributions of both the concerted process and sequential pathway C, while the red dashed rectangle with $0 \leqslant \gamma_{INT} \leqslant 50°$ includes only the contribution of pathway C. The count of pathway C is obtained by extending the count inside the red dashed rectangle to the whole range of γ_{INT}. Then the count of the concerted process is determined as the total count of this channel minus the count of pathway C. The branching ratios of concerted fragmentation and sequential pathway C are determined to be 52±10% and 48±10%, respectively.

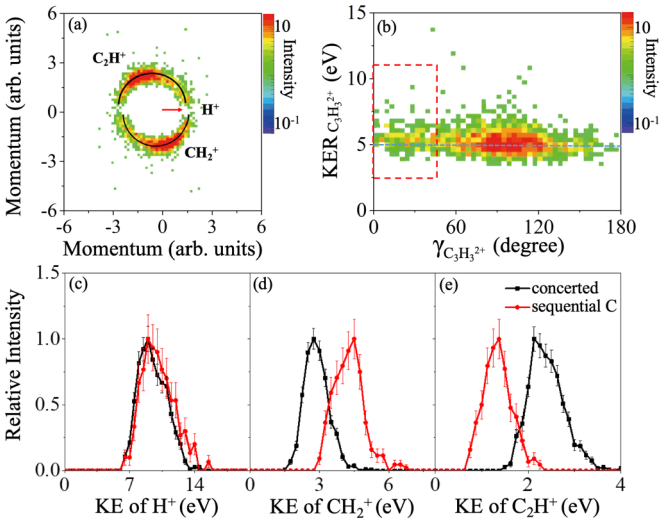

FIG. 4. (a) Newton diagram normalized to the momentum of H^+. (b)–(d) KE distributions of H^+, CH_2^+, and C_2H^+ with the Dalitz filters defined in Fig. 3(a). They are normalized to unity at the maximum. (e) The γ_{INT} vs KER_{INT} plot assuming $C_3H_3^{2+}$ as the intermediate dication. The red dashed rectangle in this figure arises exclusively from pathway C. The total count of pathway C is evaluated according to the count inside this rectangle.

C. Comparison between propyne and allene

In this part, we compare the three-body fragmentation dynamics of the two isomers. Figure 5 displays the dissociation pathways for CH_3CCH^{3+} identified in the present work (left panels) as well as for $CH_2CCH_2^{3+}$ presented in Ref. [35] (right panels). These dissociation pathways are classified according to whether the CC and CH bonds break from two distinct C atoms of the skeleton (upper panels) or from the same C atom (lower panels).

For the concerted fragmentation process, the mutual angles between three fragments strongly correlate to where the cleavage of CH and CC bonds occurred. If the CC and CH bonds break from two different C atoms of the skeleton, an intense region with the angle between the momentum vectors of H^+ and CH^+ (or CH_2^+) around 120° appears for both isomers, as shown in the upper panels of Fig. 5. This is because H^+ and CH^+ (or CH_2^+) are emitted from different ends of the C skeleton. Coulomb repulsions from the residual $C_2H_2^+$ (or C_2H^+) and between each other result in a larger mutual

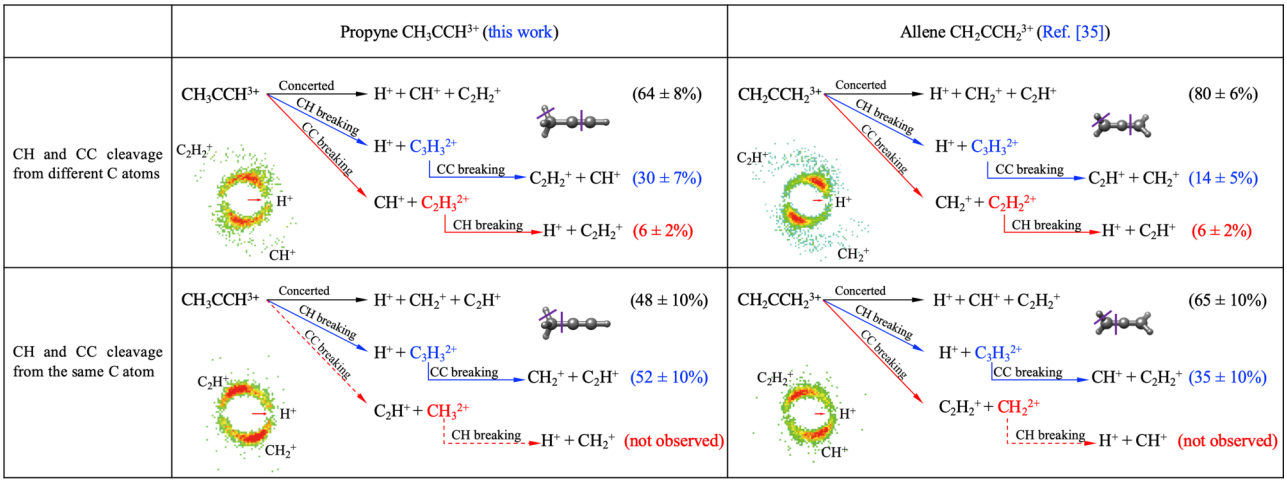

FIG. 5. Comparison between fragmentation of CH_3CCH^{3+} (left panels) and $CH_2CCH_2^{3+}$ (right panels). Upper panels for the fragmentation channels with CH and CC bonds cleavage from different C atoms, while lower panels for CH and CC bonds cleavage from the same C atom. The data of $CH_2CCH_2^{3+}$ are from Ref. [35].

angle around 120°. In contrast, this angle is 60° if the CC and CH bonds from the same C atom break simultaneously and H^+ and CH^+ (or CH_2^+) are produced form the same end of the C skeleton as displayed in the lower panels of Fig. 5.

In a sequential fragmentation process, the rotation period of the intermediate dication is on the order of ∼picoseconds. The survival time of the intermediate dication should be longer than this value to make the sequential process visualized as semicircles in the Newton diagram and the stripe structure in the Dalitz plot. Thus the metastable state with a lifetime longer than picoseconds may contribute to such sequential processes. Long-lived dications of $C_2H_2^{2+}$ [44–46], $C_2H_3^{2+}$ [27,47], and $C_3H_3^{2+}$ [47] with lifetimes ranging from ∼100 ns to microseconds have been observed experimentally. For example, the lifetime of the $^3\Sigma_g^-$ ground state of $C_2H_2^{2+}$ is measured to be 108 ns [44]. The observed sequential fragmentation pathways of both isomers probably arise from such metastable states with lifetimes ranging from ∼100 ns to microseconds.

The sequence of CC and CH breaking in the sequential fragmentation process is also observed to be strongly correlated with whether the CC and CH bonds break from two distinct C atoms or from the same C atom. The sequential pathway with CC bond breaking prior to CH breaking is only observed in the case that the CC and CH bonds break from two distinct C atoms, while it is absent when the two bonds are broken from the same C atom.

In the case of the CH and CC bonds breaking from the same C atom, the fragmentation sequence with CC breaking prior to CH breaking is not observed for both isomers. For CH_3CCH^{3+}, the CH_3^{2+} should be produced as the intermediate dication if such a fragmentation sequence can occur. However, CH_3^{2+} does not have a signifciant lifetime [48], and no long-lived CH_3^{2+} has been observed experimentally [49,50]. This explains why the sequential pathway to the $H^+ + CH_2^+ + C_2H^+$ channel with CC breaking in the first step disappears in the fragmentation of CH_3CCH^{3+}. For $CH_2CCH_2^{3+}$, both the sequential pathway of three-body fragmentation through CH_2^{2+} as the intermediate dication and the two-body dissociation channel $CH_2^{2+} + C_2H_2^+$ are not observed in our measurement. This may indicate that dissociation of $CH_2CCH_2^{3+}$ through CC breakage as the first step is unlikely to occur. In addition, the CH_2^{2+} dication is very stable since its potential minimum is deep and has a high activation barrier which makes this dication against deprotonation dissociation [48,51]. Thus, even if the first step of CC breakage occurrs, the CH breakage in CH_2^{2+} as the second step will be blocked.

In general, the fragmentation mechanisms of both isomers discussed above show similar dependence on the location of the bond cleavage. Nevertheless, the cleavage of CH and CC bonds with similar locations leads to different fragmentation channels for different isomers. In the case of CC and CH bonds breaking simultaneously from different C atoms, the fragmentation channel is $H^+ + CH^+ + C_2H_2^+$ for CH_3CCH, while it is $H^+ + CH_2^+ + C_2H^+$ for CH_2CCH_2. Once the CC and CH bonds break from the same C atom, the fragmentation channel is $H^+ + CH_2^+ + C_2H^+$ for CH_3CCH, but $H^+ + CH^+ + C_2H_2^+$ channel for CH_2CCH_2. Such differences between the two isomers are mainly determined by the CH cleavage occurring in the methyl group (CH_3) or the methylene group (CH_2).

IV. CONCLUSION

The dynamics of three-body fragmentation of CH_3CCH^{3+} to $H^+ + CH^+ + C_2H_2^+$ and $H^+ + CH_2^+ + C_2H^+$ is investigated by 50-keV/u Ne^{8+}. It is found that the concerted fragmentation with CC and CH bonds breaking simultaneously as well as the sequential fragmentation pathways with CH bond breaking prior to CC bond breaking contributes significantly to both channels. Instead, the sequential pathway with CC bond breaking in the first step followed by CH bond breaking is only observed for the $H^+ + CH^+ + C_2H_2^+$ channel. Branching ratios of different fragmentation mechanisms are estimated for each channel.

We compared the present results with the results of $CH_2CCH_2^{3+}$. The specific location of CH and CC bonds'

cleavage causes similar fragmentation mechanisms for both isomers, but results in different fragmentation channels for different isomers. In the case of CH and CC bonds breaking from distinct C atoms and the two lighter fragments emitting from different ends of the C skeleton, the concerted fragmentation leads to the mutual angle around 120° between the two lighter fragments. This angle is around 60° when the CH and CC bonds break from the same C atom and the two lighter fragments are emitted from the same end of the C skeleton. In addition, the sequential fragmentation pathway with CC breaking prior to CH is only observed in the case that the two bonds are breaking from different C atoms for both isomers, while the fragmentation sequence with CH breaking prior to CC is observed in both cases.

ACKNOWLEDGMENTS

The authors acknowledge the 320-kV platform staff at the Institute of Modern Physics, Chinese Academy of Sciences, for their technical support. The work was joint supported by the National Key Research and Development Program of China under Grant No. 2017YFA0402300 and the National Natural Science Foundation of China under Grants No. 11874365 and No. 11875219.

[1] Edited by R. Janev, *Atomic and Molecular Processes in Fusion Edge Plasmas* (Springer, New York, 1995).
[2] S. Lehnert, *Biomolecular Action of Ionizing Radiation* (CRC Press, Boca Raton, FL, 2007).
[3] P. Sada, G. Bjoraker, D. Jennings, G. McCabe, and P. Romani, Icarus **136**, 192 (1998).
[4] S. Hsieh and J. H. D. Eland, J. Phys. B: At., Mol. Opt. Phys. **30**, 4515 (1997).
[5] N. Neumann, D. Hant, L. P. H. Schmidt, J. Titze, T. Jahnke, A. Czasch, M. S. Schöffler, K. Kreidi, O. Jagutzki, H. Schmidt-Böcking, and R. Dörner, Phys. Rev. Lett. **104**, 103201 (2010).
[6] C. Wu, C. Wu, D. Song, H. Su, Y. Yang, Z. Wu, X. Liu, H. Liu, M. Li, Y. Deng, Y. Liu, L.-Y. Peng, H. Jiang, and Q. Gong, Phys. Rev. Lett. **110**, 103601 (2013).
[7] A. Khan, L. C. Tribedi, and D. Misra, Phys. Rev. A **92**, 030701(R) (2015).
[8] E. Wang, X. Shan, Z. Shen, M. Gong, Y. Tang, Y. Pan, K.-C. Lau, and X. Chen, Phys. Rev. A **91**, 052711 (2015).
[9] S. Yan, X. L. Zhu, P. Zhang, X. Ma, W. T. Feng, Y. Gao, S. Xu, Q. S. Zhao, S. F. Zhang, D. L. Guo, D. M. Zhao, R. T. Zhang, Z. K. Huang, H. B. Wang, and X. J. Zhang, Phys. Rev. A **94**, 032708 (2016).
[10] P. Bhatt, R. Singh, N. Yadav, and R. Shanker, Phys. Rev. A **86**, 052708 (2012).
[11] A. Khan, L. C. Tribedi, and D. Misra, Phys. Rev. A **96**, 012703 (2017).
[12] J. Eland, Mol. Phys. **61**, 725 (1987).
[13] M. R. Jana, B. Ray, P. N. Ghosh, and C. P. Safvan, J. Phys. B: At., Mol. Opt. Phys. **43**, 215207 (2010).
[14] K. Saha, S. Banerjee, and B. Bapat, Chem. Phys. Lett. **607**, 85 (2014).
[15] Z. Shen, E. Wang, M. Gong, X. Shan, and X. Chen, J. Chem. Phys **145**, 234303 (2016).
[16] H. Yang, M. Gong, W. Dong, Z. Shen, E. Wang, and X. Chen, J. Phys. B: At., Mol. Opt. Phys. **51**, 245201 (2018).
[17] R. Singh, P. Bhatt, N. Yadav, and R. Shanker, J. Phys. B: At., Mol. Opt. Phys. **46**, 085203 (2013).
[18] I. Ben-Itzhak, K. D. Carnes, S. G. Ginther, D. T. Johnson, P. J. Norris, and O. L. Weaver, Phys. Rev. A **47**, 3748 (1993).
[19] R. Flammini, M. Satta, E. Fainelli, G. Alberti, F. Maracci, and L. Avaldi, New J. Phys. **11**, 083006 (2009).
[20] Y. Zhang, T. Jiang, L. Wei, D. Luo, X. Wang, W. Yu, R. Hutton, Y. Zou, and B. Wei, Phys. Rev. A **97**, 022703 (2018).
[21] R. Thissen, J. Delwiche, J. Robbe, D. Duflot, J.-P. Flament, and J. Eland, J. Chem. Phys. **99**, 6590 (1993).
[22] A. Hishikawa, A. Matsuda, M. Fushitani, and E. J. Takahashi, Phys. Rev. Lett. **99**, 258302 (2007).
[23] S. De, J. Rajput, A. Roy, P. N. Ghosh, and C. P. Safvan, Phys. Rev. A **77**, 022708 (2008).
[24] S. Xu, X. L. Zhu, W. T. Feng, D. L. Guo, Q. Zhao, S. Yan, P. Zhang, D. M. Zhao, Y. Gao, S. F. Zhang, J. Yang, and X. Ma, Phys. Rev. A **97**, 062701 (2018).
[25] T. Jiang, B. Wang, Y. Zhang, L. Wei, S. Chen, W. Yu, Y. Zou, L. Chen, and B. Wei, Phys. Rev. A **100**, 022705 (2019).
[26] S.-H. Lee, Y. Lee, and X. Yang, J. Chem. Phys. **120**, 10983 (2004).
[27] X. Xie, E. Lötstedt, S. Roither, M. Schöffler, D. Kartashov, A. Baltuška, K. Yamanouchi, and M. Kitzler, Sci. Rep. **5**, 12877 (2015).
[28] P. J. Richardson, J. H. D. Eland, and P. Lablanquie, Org. Mass Spectrom. **21**, 289 (1986).
[29] A. Matsuda, M. Fushitani, R. Thomas, V. Zhaunerchyk, and A. Hishikawa, J. Phys. Chem. A **113**, 2254 (2009).
[30] Y. Nakano, M. Hoshino, M. Kitajima, H. Tanaka, and M. Kimura, Phys. Rev. A **66**, 032714 (2002).
[31] T. Kusakabe, S. Satoh, H. Tawara, and M. Kimura, Phys. Rev. Lett. **87**, 243201 (2001).
[32] S. W. J. Scully, V. Senthil, J. A. Wyer, M. B. Shah, E. C. Montenegro, M. Kimura, and H. Tawara, Phys. Rev. A **72**, 030701(R) (2005).
[33] Y. Li, S. Xu, D. Guo, S. Jia, X. Jiang, X. Zhu, and X. Ma, J. Chem. Phys. **150**, 144311 (2019).
[34] H. Yuan, S. Xu, T. Li, Y. Liu, D. Qian, D. Guo, X. Zhu, and X. Ma, Phys. Rev. A **102**, 062808 (2020).
[35] C. Ma, S. Xu, D. Zhao, D. Guo, S. Yan, W. Feng, X. Zhu, and X. Ma, Phys. Rev. A **101**, 052701 (2020).
[36] R. Dörner, V. Mergel, O. Jagutzki, L. Spielberger, J. Ullrich, R. Moshammer, and H. Schmidt-Böcking, Phys. Rep. **330**, 95 (2000).
[37] J. Ullrich, R. Moshammer, A. Dorn, R. Dörner, L. P. H. Schmidt, and H. Schmidt-Böcking, Rep. Prog. Phys. **66**, 1463 (2003).
[38] X. Ma, R. T. Zhang, S. F. Zhang, X. L. Zhu, W. T. Feng, D. L. Guo, B. Li, H. P. Liu, C. Y. Li, J. G. Wang, S. C. Yan, P. J. Zhang, and Q. Wang, Phys. Rev. A **83**, 052707 (2011).

[39] R. Dalitz, Proc. Phys. Soc., Sect. A **66**, 710 (2002).
[40] R. H. Dalitz, Phys. Rev. **94**, 1046 (1954).
[41] J. Rajput, T. Severt, B. Berry, B. Jochim, P. Feizollah, B. Kaderiya, M. Zohrabi, U. Ablikim, F. Ziaee, K. Raju, P. D. Rolles, A. Rudenko, K. D. Carnes, B. D. Esry, and I. Ben-Itzhak, Phys. Rev. Lett. **120**, 103001 (2018).
[42] H. Kumar, P. Bhatt, C. P. Safvan, and J. Rajput, J. Chem. Phys. **148**, 064302 (2018).
[43] Y. Wang, X. Shi, J. Zhou, S. Xu, D. Guo, S. Yan, X. Zhu, and X. Ma, Phys. Rev. A **101**, 042706 (2020).
[44] M. Alagia, C. Callegari, P. Candori, S. Falcinelli, F. Pirani, R. Richter, S. Stranges, and F. Vecchiocattivi, J. Chem. Phys. **136**, 204302 (2012).
[45] B. Wolter, M. G. Pullen, A.-T. Le, M. Baudisch, K. Doblhoff-Dier, A. Senftleben, M. Hemmer, C. D. Schröter, J. Ullrich, T. Pfeifer, R. Moshammer, S. Gräfe, O. Vendrell, C. D. Lin, and J. Biegert, Science **354**, 308 (2016).
[46] S. Larimian, S. Erattupuzha, E. Lötstedt, T. Szidarovszky, R. Maurer, S. Roither, M. Schöffler, D. Kartashov, A. Baltuška, K. Yamanouchi, M. Kitzler, and X. Xie, Phys. Rev. A **93**, 053405 (2016).
[47] L. Wei, B. Ren, Y. Zhang, J. Wang, B. Wang, J. Han, W. Yu, Y. Zou, L. Chen, and B. Wei, Phys. Rev. A **103**, 012810 (2021).
[48] J. A. Pople, B. Tidor, and P. von Ragué Schleyer, Chem. Phys. Lett. **88**, 533 (1982).
[49] Z. Wu, C. Wu, Q. Liang, S. Wang, M. Liu, Y. Deng, and Q. Gong, J. Chem. Phys. **126**, 074311 (2007).
[50] M. Sharifi, F. Kong, S. L. Chin, H. Mineo, Y. Dyakov, A. M. Mebel, S. D. Chao, M. Hayashi, and S. H. Lin, J. Phys. Chem. A **111**, 9405 (2007).
[51] Y. Levy, A. Bar-David, I. Ben-Itzhak, I. Gertner, and B. Rosner, J. Phys. B: At., Mol. Opt. Phys. **32**, 3973 (1999).